# The LSND and MiniBooNE Oscillation Searches at High $\Delta m^2$

Janet M. Conrad

*Massachusetts Institute of Technology; Cambridge, MA 02139*

William C. Louis

*Los Alamos National Laboratory; Los Alamos, NM 87545*

Michael H. Shaevitz

*Columbia University; New York, NY 10027*



**Abstract**

This paper reviews the results of the LSND and MiniBooNE experiments. The primary goal of each experiment was to effect sensitive searches for neutrino oscillations in the mass region with $\Delta m^2 \sim 1$ eV$^2$. The two experiments are complementary, and so the comparison of results can bring additional information with respect to models with sterile neutrinos. Both experiments obtained evidence for $\bar{\nu}_\mu \to \bar{\nu}_e$ oscillations, and MiniBooNE also observed a $\nu_\mu \to \nu_e$ excess. In this paper, we review the design, analysis, and results from these experiments. We then consider the results within the global context of sterile neutrino oscillation models. The final data sets require a more extended model than the simple single sterile neutrino model imagined

at the time that LSND drew to a close and MiniBooNE began. We show that there are apparent incompatibilities between data sets in models with two sterile neutrinos. However, these incompatibilities may be explained with variations within the systematic error. Overall, models with two (or three) sterile neutrinos seem to succeed in fitting the global data, and they make interesting predictions for future experiments.

## CONTENTS

## 1 Introduction

In the past 20 years, neutrino oscillations–where a beam of one flavor of neutrino evolves to have components of other flavors–have gone from speculation to demonstration. This has motivated an extension to particle physics phenomenology that includes finite neutrino masses and a (3×3) mixing matrix that connects the three known neutrino flavors, $\nu_e$, $\nu_\mu$, and $\nu_\tau$, to the three mass states, $\nu_1$, $\nu_2$, and $\nu_3$ (1). However, this extension may not be the entire story. Indeed, experimental clues are arising that seem to point to additional, noninteracting ("sterile") neutrino states. Among the experimental results, the LSND and MiniBooNE experiments have been crucial motivators for the recent explosion of interest in this topic (2). This excitement in the community, as well as the end of MiniBooNE running in 2012, provides the *raison d'etre* for a review of the LSND and MiniBooNE results at this time.

To understand why richer phenomenology is motivated, one must consider the observed "mass splittings" measured in neutrino oscillation experiments. These are the differences between the squared mass values. A model with three neutrinos will have two independent mass splittings. In the presently accepted picture of neutrino oscillations, the magnitude of the mass splitting between $\nu_1$ and $\nu_2$ is $\Delta m^2_{21} = (7.50 \pm 0.185) \times 10^{-5}$ eV$^2$, and $\nu_2$ and $\nu_3$ is $\Delta m^2_{32} = (2.47^{+0.069}_{-0.067}) \times 10^{-3}$ eV$^2$ (1). However, experimental results indicate $> 3\sigma$ evidence for oscillations with $\Delta m^2 \sim 1$ eV$^2$. A way to accommodate this higher mass splitting is the introduction of sterile neutrinos that act as new flavors that mix with the Standard Model flavors but do not couple to the $W$ or $Z$, thereby avoiding the limits on extra active neutrino flavors (3).

This paper focuses primarily on LSND and MiniBooNE, two experiments that

were constructed to probe the $\Delta m^2 \sim$1 eV$^2$ region. In 1995, LSND was the first experiment to publish evidence for a signal at $\Delta m^2 \sim 1$ eV$^2$, observing $\bar{\nu}_\mu \to \bar{\nu}_e$ (4,5,6,7). MiniBooNE was proposed (8) in 1998 to follow up on this signal, while substantially changing the systematics. MiniBooNE saw excesses in $\nu_\mu \to \nu_e$ and $\bar{\nu}_\mu \to \bar{\nu}_e$ modes (9, 10, 11).

This paper examines the LSND and MiniBooNE appearance signals. We begin, in Sec. 2, by discussing the oscillation phenomenology that will be used throughout the paper. In Sec. 3 we introduce the LSND and MiniBooNE experiments, drawing important distinctions between the designs. The primary results of the experiments, the appearance signals, are presented in Sec. 4. LSND and MiniBooNE have also reported $\nu_e$ and $\nu_\mu$ disappearance limits, and other experiments sensitive to the $\Delta m^2 \sim 1$ eV$^2$ region have presented relevant results as well. The LSND and MiniBooNE appearance signal cannot be interpreted outside of consideration of these other data sets, which we report in Sec. 5. Then, in Sec. 6, we end by using those data sets, to explore potential sterile neutrino models that may explain the LSND and MiniBooNE results. We make the case that models with at least two additional sterile states, and that include $CP$ violation, can successfully describe all of the data sets. These models are testable in the near future.

## 2 Phenomenology of Oscillations Involving Sterile Neutrinos

We will interpret LSND, MiniBooNE, and other experimental results within neutrino oscillation models. Oscillations arise if neutrinos are produced, through weak decay, in a specific flavor eigenstate that is a combination of mass eigenstates. The mass eigenstates propagate with slightly different frequencies, leading

to neutrino-flavor probability waves with oscillating beats among the flavors.

In a simple two-neutrino model, the flavor states, $\nu_e$ and $\nu_\mu$, are linked to the mass states, $\nu_1$ and $\nu_2$, via a mixing matrix that is a simple rotation matrix. At $t = 0$, the neutrinos are described by:

$$|\nu_e\rangle = \cos\theta\ |\nu_1\rangle + \sin\theta\ |\nu_2\rangle \text{ and} \tag{1}$$

$$|\nu_\mu\rangle = -\sin\theta\ |\nu_1\rangle + \cos\theta\ |\nu_2\rangle, \tag{2}$$

where $\theta$ is called the "mixing angle." The quantum mechanical interference of the mass eigenstates as they propagate leads to the appearance oscillation probability:

$$P = \sin^2 2\theta\ \ \sin^2(1.27\Delta m^2(L/E)), \tag{3}$$

where $\theta$ is the mixing angle, $L$, in m, is the distance from production to detection, $E$, in MeV, is the energy of the neutrino, and $\Delta m^2 = m_2^2 - m_1^2$, in eV$^2$, is the mass splitting. The disappearance probability is given by

$$P = 1 - \sin^2 2\theta\ \ \sin^2(1.27\Delta m^2(L/E)). \tag{4}$$

From the above, one sees that for LSND and MiniBooNE to be sensitive to $\Delta m^2 \sim 1$ eV$^2$, one chooses $L/E \sim 1$ m/MeV to maximize the oscillation probability. Because typical beam energies range from a few MeV to a few GeV, this $L/E$ demands experiments that are relatively close to the site of neutrino production. As a result, these are called "short baseline" (SBL) experiments.

Any single SBL experiment is likely to fit well within this simple two-neutrino model, producing either a signal or a limit at a given confidence level (CL). However, adding additional data sets generally requires extensions to more than two flavors. The phenomenological extension to three active neutrinos provides an example of how to enlarge the model (1). In a series of recent papers, we have

explored how to take the next step of also introducing sterile netrinos states(12, 13,14). Reference (15) provides a good step-by-step review of the ideas which we summarize briefly here.

The simplest extension is the "3+1 model," which introduces one sterile neutrino, labeled "s," that can mix with the three active flavors. This leads to a mixing matrix that connects the 3+1 flavors to four mass states:

$$\begin{pmatrix} \nu_e \\ \nu_\mu \\ \nu_\tau \\ \nu_s \end{pmatrix} = \begin{pmatrix} U_{e1} & U_{e2} & U_{e3} & U_{e4} \\ U_{\mu 1} & U_{\mu 2} & U_{\mu 3} & U_{\mu 4} \\ U_{\tau 1} & U_{\tau 2} & U_{\tau 3} & U_{\tau 4} \\ U_{s1} & U_{s2} & U_{s3} & U_{s4} \end{pmatrix} \begin{pmatrix} \nu_1 \\ \nu_2 \\ \nu_3 \\ \nu_4 \end{pmatrix}.$$

The mixing among the three active flavor states is highly constrained by measurements from Daya Bay (16), Double Chooz (17), KamLAND (18), MINOS (19,20), RENO (21), Super K (22), SNO (23), and T2K (24, 25). Accommodating these data requires that three of the mass states be mostly active flavors, which leads to the fourth mass state, $\nu_4$, being primarily sterile. This model assumes that $|U_{\tau 4}|$ is negligible, for simplicity. The "SBL approximation," $\Delta m^2_{21} \approx \Delta m^2_{31} \equiv 0$, is applied, motivated by the assumption that the $\nu_4$ mass is much larger than the other mass states. As a result, the $\nu_\mu \rightarrow \nu_e$ appearance probability simplifies to Eq. 3, with $\sin^2 2\theta$ given by

$$\sin^2 2\theta_{e\mu} = 4U^2_{e4}U^2_{\mu 4}. \tag{5}$$

The disappearance probabilities are given by Eq. 4 with

$$\sin^2 2\theta_{\mu\mu} = 4U^2_{\mu 4}(1 - U^2_{\mu 4}) \quad (\mu\ flavor), \tag{6}$$

$$\sin^2 2\theta_{ee} = 4U^2_{e4}(1 - U^2_{e4}) \quad (e\ flavor). \tag{7}$$

From these equations, one sees that a successful 3+1 model has two require-

ments: 1) that individual appearance and disappearance data sets be well described by Eqs. 3 and 4, and 2) that all of the data sets together map onto the same three parameters: $U_{e4}$, $U_{\mu 4}$, and $\Delta m^2_{41}$. We will show in Sec. 6.1 that the LSND and MiniBooNE results fit poorly within a global 3+1 analysis.

This motivates extension to a 3+2 model, with two sterile states and seven oscillation parameters. In addition to the three parameters from 3+1, the 3+2 model introduces an extra mass splitting, $\Delta m^2_{51}$, the mixing elements, $|U_{e5}|$ and $|U_{\mu 5}|$, and a complex phase, $\phi_{54}$. The complex phase allows for significant $CP$ violation, manifested as a difference between the neutrino and antineutrino appearance oscillation probabilities. However, because this is an interference effect, $CP$ violation will only be significant if $\Delta m^2_{51}/\Delta m^2_{41} \lesssim \mathcal{O}(10)$. $CP$ violation will allow the signal for neutrino oscillations to be softer than for antineutrino oscillations, which we will show is preferred by the MiniBooNE data in Sec. 6.2.

Three sterile neutrino states, one for each active flavor generation, seems most natural. However, a 3+3 model is not found to significantly improve on the 3+2 fits, and the conclusions are very similar. Therefore, for lack of space, we do not include a discussion of 3+3 phenomenology or fits. Interested readers should see Ref. (15).

## 3 Comparing The LSND and MiniBooNE Experiments

Although both LSND and MiniBooNE had $L/E \sim 1$ m/MeV to probe $\Delta m^2 \sim 1$ eV$^2$, the designs were quite different. MiniBooNE used a beam which was an order of magnitude higher in energy than that of LSND, leading to different event signatures, backgrounds, and systematic uncertainties. Correspondingly, MiniBooNE was located a distance that was approximately an order of magnitude

farther from the neutrino source. For a brief comparison, see Table 1.

### 3.1 LSND

The LSND beam was produced at the Los Alamos National Laboratory LAMPF/LANSCE accelerator. A 1 mA proton beam at 798 MeV impinged on the target/dump system with duty factor of $6 \times 10^{-2}$ (7) to produce pions and muons that decayed at rest. The decay-at-rest (DAR) neutrino flux, shown in Fig. 1, arises from stopped $\pi^+ \to \nu_\mu \mu^+$ decay followed by stopped $\mu^+ \to \bar{\nu}_\mu \nu_e e^+$. The sister decay chain from stopped $\pi^-$ is highly suppressed through pion capture on target nuclei. The $\bar{\nu}_e$ intrinsic background at LSND was only $\sim 8 \times 10^{-4}$ of the $\bar{\nu}_\mu$ flux in the energy range of the analysis (26).

The $\bar{\nu}_e$ in the beam, either due to signal or background, could interact via "inverse beta decay" (IBD), $\bar{\nu}_e p \to e^+ n$, in the mineral oil target of the LSND detector. This reaction has a twofold signature of a prompt positron and a correlated 2.2 MeV $\gamma$ from neutron capture. Although the target oil was lightly doped with scintillator, the Cherenkov ring could still be reconstructed, allowing the determination of the energy and angle of the outgoing positron. The $\nu_\mu$ and $\bar{\nu}_\mu$ energies were below threshold for charged-current (CC) muon production; thus, only neutral-current (NC) events were produced. The $\nu_e$ in the beam produced $\nu_e + {}^{12}\mathrm{C} \to {}^{12}\mathrm{N}_{gs} + e^-$ events, where *gs* indicates ground state. This was not confused with the IBD signal, as there was no correlated neutron capture in these events. The $\nu_e$ events were used in a disappearance study discussed in Sec. 5.1.

Fig. 2 illustrates the LSND detector (27), which consisted of a cylindrical tank, 8.3 m long by 5.7 m in diameter with center located 29.8 m from the neutrino source. 1220 8-inch Hamamatsu photomultiplier tubes (PMTs) covered 25% of

the tank surface area. The tank was filled with 167 tons of liquid scintillator consisting of mineral oil and 0.031 g/l of b-PBD. A typical 45-MeV electron from a CC interaction produced $\sim 1500$ photoelectrons, of which $\sim 280$ photoelectrons were in the Cherenkov cone. PMT time and pulse-height signals were used to reconstruct the track with an average RMS position resolution of $\sim 14$ cm, an angular resolution of $\sim 12^\circ$, and an energy resolution of $\sim 7\%$ at the Michel electron endpoint of 52.8 MeV.

The veto shield, consisting of a 15-cm layer of liquid scintillator in an external tank and 15 cm of lead shot in an internal tank, enclosed the detector on all sides except the bottom (28). The active veto tagged cosmic-ray muons that stopped in the lead shot. Additional counters were placed below the tank after the 1993 run to reduce cosmic-ray background entering through the bottom support structure. A veto inefficiency $< 10^{-5}$ was achieved for incident charged particles, and the veto introduced a $0.76 \pm 0.02$ deadtime.

### 3.2 MiniBooNE

In contrast to LSND, MiniBooNE made use of a "conventional neutrino beam" at Fermilab where protons hit a target and produce mesons that decay in flight. The Booster accelerator fed 8-GeV kinetic energy protons to a 71-cm long Be target located at the upstream end of a magnetic focusing horn. The horn pulsed with a current of 174 kA. Depending on the polarity, this either focused $\pi^+$ and $K^+$ or $\pi^-$ and $K^-$ into a 50-m decay pipe. The neutrinos or antineutrinos produced from the meson decays could interact in the MiniBooNE detector, located 541 m downstream of the Be target.

Fig. 3 shows the neutrino fluxes for this Booster Neutrino Beam (BNB) used by

MiniBooNE, for neutrino mode and antineutrino mode running (29). The fluxes are fairly similar for the two modes, both in energy and in the intrinsic electron-neutrino background, which is ∼0.6%. However, as with all conventional neutrino beams, the wrong-sign contribution to the flux in antineutrino mode (∼ 18%) is much larger than in neutrino mode (∼ 6%).

MiniBooNE (30) utilized a 12.2-m diameter spherical tank filled with 806 tons of mineral oil ($CH_2$) with no scintillator doping, shown schematically in Fig. 4. A total of 1280 8-inch PMTs covered 10% of the surface area of the target region, which was painted black to reduce reflections. The fiducial volume within the target had a 5-m radius and corresponded to 450 tons. The target region was optically isolated from a full-coverage veto that was 30 cm thick and contains 240 veto PMTs. White reflective paint on the veto walls led to high reflection and excellent efficiency for cosmic-muon detection of $> 99.9\%$.

At BNB energies, the important contributions to the neutrino and antineutrino CC cross sections are quasi-elastic (QE) scattering and single pion production, typically from $\Delta$ baryon production. A review of these interactions is provided in Ref. (31), and we note that MiniBooNE has provided a great deal of new data related to the cross-section measurements. The targets were nucleons in the carbon atoms and free protons associated with the hydrogen atoms. Signal identification and background rejection relied on the measured characteristics of the observed Cherenkov rings. As a result, the analysis proceeded quite differently to that of LSND. A key aspect of MiniBooNE is that the backgrounds are very well understood and are constrained directly from measurements in the detector as described below.

## 4 Appearance Results from LSND and MiniBooNE

Both the LSND and MiniBooNE experiments have reported muon-flavor to electron-flavor appearance signals. This section will show that the results of each search are individually consistent with the two-flavor oscillation phenomenology introduced in Sec. 2. However, in Sec. 6 we show that an extended model is required to explain the combined data sets.

### 4.1 LSND

LSND presented a number of incremental results throughout the run (4, 5, 6), and the final results were presented in a comprehensive paper in 2001 (7). In this section, we mainly review the primary oscillation analysis but briefly consider several cross-check analyses performed to address the consistency of the result.

4.1.1 LSND Oscillation Analysis Due to the poor duty factor, the raw event sample of LSND had a high cosmic-ray content, and so initial "Reduction Criteria" were applied. The first step was a prompt energy requirement of $E_e >$ 20 MeV. Timing cuts on target and veto shield activity further reduced the cosmic background. Next, "Electron Selection Criteria" were applied. These cuts isolated candidate events in time, required a reconstructed event vertex greater than 35 cm from the faces of the PMTs, and selected on particle ID parameters derived from the position and timing of PMT hits as described in Ref. (7). The analysis also required $E_e < 60$ MeV to isolate the DAR sample from decay-in-flight events. From the tagged Michel electron sample from cosmic-muon decay, the efficiency for the Electron Selection was $0.42 \pm 0.03$.

Next, the coincidence with a 2.2 MeV $\gamma$ from neutron capture was required. The task was to distinguish true neutron captures from accidental $\gamma$s from ra-

dioactivity. To this end, LSND introduced the ratio, $R_\gamma$, of the likelihood that the $\gamma$ is correlated divided by the likelihood that the $\gamma$ is accidental, which depended upon three quantities: the number of hit PMTs, since the multiplicity is proportional to the $\gamma$ energy; the distance between the reconstructed $\gamma$ position and positron-candidate position; and the time interval between the $\gamma$ and positron candidate.

The $R_\gamma$ distribution of the events passing Electron Selection was fit to templates of the correlated signal and accidental backgrounds with floating normalization, yielding a $\chi^2/\mathrm{dof} = 10.7/9$. From this, $117.9 \pm 22.4$ $\bar{\nu}_e$ events were found to be in the sample. Of these, $19.5 \pm 3.9$ and $10.5 \pm 4.6$ are predicted to be from intrinsic $\bar{\nu}$ sources from $\mu^-$ decay at rest and $\pi^-$ decay in flight, respectively (32). Thus, the LSND signal excess corresponds to $87.9 \pm 22.4 \pm 6.0$ events. For comparison, from the expected candidate rate with 100% transmutation of the $\bar{\nu}_\mu$ flux, one expects $33,300 \pm 3,300$ events. Interpreting the excess as oscillations in a two-neutrino model, the probability is $(0.264 \pm 0.067 \pm 0.045)\%$.

Using Eq. 3, a fit is performed for $\bar{\nu}_\mu \rightarrow \bar{\nu}_e$ appearance by calculating the likelihood ($\mathcal{L}$) in the $(\sin^2 2\theta, \Delta m^2)$ plane to extract the favored oscillation parameters. The three-dimensional contour in $(\sin^2 2\theta, \Delta m^2, \mathcal{L})$ is sliced to find the LSND allowed oscillation region. The result is shown in Fig. 5, where the inner (outer) region corresponds to a 90% (99%) CL.

In the same timeframe as the LSND run, the KARMEN experiment (33) took data with a DAR beam at the ISIS facility at the Rutherford Laboratory. A key difference with respect to LSND is the KARMEN location at 17.7 m from the target at a 100° angle to the proton beam. KARMEN did not observe an oscillation signal (34) and obtained the 90% CL limit shown in Fig. 5. KARMEN

restricts part of the LSND region and, through a joint analysis with LSND, was used to determine a combined allowed region for the two experiments (35).

The most controversial cuts in the DAR analysis have been those on the fiducial volume. Questions arose because of an apparent up-down asymmetry in the first LSND result, presented in 1995. The result, which also used a stricter energy cut, $E_e > 36$ MeV, than the final analysis, had only nine candidate events, with six at $Y < 0$ and three at $Y > 0$ (4). Although this is not a highly improbable $Y$ distribution, concern was raised because the top of the detector had complete veto coverage, while the bottom did not. Continued running smoothed the statistical fluctuation. Table 2 provides the oscillation probabilities for the final event sample with exercises in varying the fiducial cuts, showing that the signal is resilient to these cuts.

Another useful cross-check maintains the Electron Selection cuts but employs an $R_\gamma > 10$ cut rather than the template fit. This isolates a very clean signal, revealing the hallmark $L/E$ distribution evident in Fig. 6. The event excess is $32.2 \pm 9.4 \pm 2.3$ and the probability that this is a statistical fluctuation is $1.1 \times 10^{-4}$.

### 4.2 MiniBooNE

The MiniBooNE experiment ran for ten years, from 2002 until 2012, switching between neutrino and antineutrino mode running. The final data sample corresponds to $6.46 \times 10^{20}$ ($11.27 \times 10^{20}$) protons on target (POT) in neutrino (antineutrino) mode. MiniBooNE searched for $\nu_\mu \to \nu_e$ (or $\bar{\nu}_\mu \to \bar{\nu}_e$) oscillations by measuring the rate of $\nu_e n \to e^- p$ (or $\bar{\nu}_e p \to e^+ n$) charged-current quasi-elastic (CCQE) events and testing whether the measured rate was consistent with the estimated background rate. For these events, the incoming $\nu/\bar{\nu}$ energy is approx-

imated according to the QE formula:

$$E^{QE}_{\nu_{mode}/\bar{\nu}_{mode}} = \frac{2(M'_{n/p})E_e - ((M'_{n/p})^2 + m_e^2 - M^2_{p/n})}{2[(M'_{n/p}) - E_e + \sqrt{E_e^2 - m_e^2}\cos\theta_e]}, \quad (8)$$

where $M_n$, $M_p$, and $m_e$ are the neutron, proton, and electron masses, and $E_e$ and $\cos\theta_e$ are the energy and angle of the outgoing electron, respectively. The adjusted neutron/proton mass is defined as $M'_{n/p} = M_{n/p} - E_B$, with binding energy $E_B = 34 \pm 9$ MeV.

A number of papers were published over this period documenting the oscillation analyses with various data samples and stages of analysis. The first oscillation publication was in 2007 (9) on the neutrino mode search, and it showed that there was no excess of events with $E_\nu^{QE} > 475$ MeV, which was somewhat inconsistent with the LSND result for antineutrinos. This was followed by a paper in 2009 (36) showing that there was an unexplained excess of $\nu_e$ events for MiniBooNE neutrino running below 475 MeV, prompting speculations of $CP$ violation such as that included in 3+2 models. At this point, MiniBooNE switched to mainly antineutrino mode running, with early results presented in 2009 (10) and 2010 (37). The antineutrino oscillation results for the full data sample were recently posted (11) and show an antineutrino excess consistent with the LSND signal region.

4.2.1 MiniBooNE Oscillation Analysis The MiniBooNE oscillation search can be broken into two main components. The first component uses analysis cuts to isolate a fairly pure sample of electron neutrino events, and the second component uses background estimates and measurements to determine the size and uncertainty of a possible excess from oscillations. The main backgrounds to a $\nu_e$ oscillation signal can be divided into two types: 1) single $\gamma$ events that mimic an outgoing electron and 2) intrinsic $\nu_e$-induced events that are identi-

cal to the oscillation signal. The single $\gamma$ backgrounds are important since the MiniBooNE detector cannot separate events with a single $\gamma$ from those with an outgoing electron. These backgrounds include NC $\pi^0$ events where one of the decay $\gamma$ rays is unobserved, radiative $\Delta \rightarrow N\gamma$ events, and $\gamma$'s from external neutrino interactions outside of the detector. The intrinsic $\nu_e$ backgrounds are from the decays of secondary muons plus charged and neutral kaons produced in the primary production target and shielding.

To select candidate $\nu_e$ CCQE events, an initial selection is first applied: $> 200$ tank hits, $< 6$ veto hits, reconstructed time within the neutrino beam spill, reconstructed vertex radius $< 500$ cm, and visible energy $E_{vis} > 140$ MeV. With these cuts, the cosmic-ray backgrounds are negligible. It is then required that the event vertex be reconstructed assuming an outgoing electron and the track endpoint reconstructed assuming an outgoing muon occur at radii $< 500$ cm and $< 488$ cm, respectively, to ensure good event reconstruction and efficiency for possible muon decay electrons. One remaining background from neutrino interactions in the material surrounding the detector is substantially reduced using correlated energy and topology cuts, and the subsequent rate is measured from isolated background events that have low energy, large radius, and a topology that points into the detector.

After the selection cuts, the surviving events are reconstructed under four hypotheses: a single electron-like Cherenkov ring, a single muon-like ring, two photon-like rings with unconstrained kinematics, and two photon-like rings consistent with the decay of a $\pi^0$. The assessment of detector response to these hypotheses uses a detailed model of extended-track light production and propagation in the tank to predict the charge and time of hits on each PMT. This

reconstruction yields a position, direction, and energy resolution for $\nu_e$ events of 22 cm, 2.8°, and 11%, respectively, and a $\pi^0$ mass resolution of 20 MeV/c$^2$.

Particle identification (PID) cuts are then applied to reject muon and $\pi^0$ events. The PID uses energy-dependent cuts on the likelihood ratios for the four above hypotheses, specifically $\log(L_e/L_\mu)$, $\log(L_e/L_{\pi^0})$, and $M_{\gamma\gamma}$. These PID cuts substantially reduce the $\gamma$ backgrounds but have a high efficiency ($55 \pm 3\%$) for $\nu_e$-induced events.

All of the MiniBooNE backgrounds are constrained by *in-situ* measurements. The $\nu_\mu$ inclusive CC background is verified by comparing the Monte Carlo (MC) prediction to the large sample of tagged events with a Michel decay electron. Over 99% of the NC $\pi^0$ events are correctly reconstructed as two $\gamma$ from $\pi^0$ decay and can be used to constrain the background where one $\gamma$ is missed. This sample can also be used to constrain the radiative $\Delta \to N\gamma$ background. The intrinsic $\nu_e$ background events from muon decay are directly related to the observed $\nu_\mu$ events since both come from a common $\pi^\pm$ decay chain. MiniBooNE uses a combined fit of the observed $\nu_\mu$ and $\nu_e$ events, including correlations, to effect this constraint. The other major source of background $\nu_e$ events is $K^+$ decay, where the $K^+$ rate has been measured using the high-energy events in the SciBooNE detector located near the end of the BNB decay pipe (38).

Table 3 shows the expected number of candidate $\nu_e$ and $\bar{\nu}_e$ CCQE background events with $E_\nu^{QE}$ between $200 - 1250$ MeV after the complete event selection of the final analysis. After applying the above mentioned $\nu_\mu$ constraint, the total expected backgrounds for neutrino mode and antineutrino mode are $790.0 \pm 28.1 \pm 38.7$ and $399.6 \pm 20.0 \pm 20.3$ events, respectively, where the first (second) error is statistical (systematic). The number of data events after all cuts is 952 for

neutrino mode and 478 for antineutrino mode, giving data excesses of $162 \pm 47.8$ and $78.4 \pm 28.5$ events for the two modes, where the error includes both statistical and systematics uncertainties.

Fig. 7 shows the reconstructed neutrino and antineutrino energy distributions for candidate $\nu_e$ and $\bar{\nu}_e$ data events (points with error bars) compared to the MC simulation (histogram with systematic uncertainties) (11). Fig. 8 shows the event excess as a function of reconstructed neutrino energy. For the neutrino data, the magnitude of the excess is similar to that expected from the LSND antineutrino oscillation signal, but the shape shows a decided difference, being larger below 400 MeV and much smaller above 500 MeV. The lack of a significant excess above 475 MeV is the source of the original MiniBooNE claim of incompatibility with LSND. In contrast, the antineutrino excess shows a similar magnitude and shape with respect to the LSND predictions and is fully consistent with the LSND signal.

The MiniBooNE neutrino and antineutrino data can be fit to a two-neutrino oscillation model, where the probability is given by Eq. 3. The $\nu_e$ fit is constrained by the observed $\nu_\mu$ data by doing a combined fit of the observed $E_\nu^{QE}$ event distributions for muon-like and electron-like events. The fit assumes the same oscillation probability for both the right-sign $\bar{\nu}_e$ and wrong-sign $\nu_e$ and no significant $\nu_\mu$, $\bar{\nu}_\mu$, $\nu_e$, or $\bar{\nu}_e$ disappearance. Using a likelihood-ratio technique (37), the CL critical values for the fitting statistic $\Delta\chi^2 = \chi^2(point) - \chi^2(best)$ as a function of the oscillation parameters $\Delta m^2$ and $\sin^2 2\theta$ are determined from frequentist fake data studies. Fig. 9 shows the MiniBooNE contours for $\nu_e$ and $\bar{\nu}_e$ appearance oscillations in the $200 < E_\nu^{QE} < 3000$ MeV energy range. The data indicate an oscillation signal region at greater than 95% CL (99% CL) with

respect to a no-oscillation hypothesis for neutrino (antineutrino) mode. In neutrino mode, the MiniBooNE favored region is somewhat below the LSND allowed region, but in antineutrino mode the MiniBooNE region is consistent with large parts of the LSND 99% CL allowed region and consistent with the limits from the KARMEN experiment (34).

## 5 Data Sets for Global Fits at High $\Delta m^2$

The LSND and MiniBooNE appearance results must be considered within the context of other relevant oscillation limits and signals. Indeed, both LSND and MiniBooNE data provide disappearance limits that are important constraints for global fits. Here we consider these disappearance results, as well as results from other SBL experiments.

### 5.1 LSND and MiniBooNE Disappearance Searches

Both the LSND and the MiniBooNE data sets can also be used for disappearance searches, in which the neutrinos oscillate to flavors that are not observed in the detector. In such a search, the highest precision is achieved with a "near detector" that constrains the unoscillated flux. Therefore, for these analyses, LSND and MiniBooNE had to be paired with sister experiments at closer distances– KARMEN (34) and SciBooNE (40), respectively.

Both the LSND and KARMEN experiments made accurate measurements of the $\nu_e$-carbon cross section in the range $20 < E_e < 60$ MeV using the reaction $\nu_e + {}^{12}C \rightarrow {}^{12}N_{gs} + e^-$ (41, 42). The cross section is measured by dividing the event rate by the predicted DAR flux, assuming no oscillations and with appropriate normalizations. Since KARMEN and LSND were at different distances

from their neutrino sources, $\nu_e$ disappearance oscillations can induce a difference in the measured cross sections. By comparing the measured cross sections, accounting for normalization uncertainties (43, 44) and using the respective $L$ values, restrictions on the allowed oscillation parameters (45) are obtained.

MiniBooNE has also performed $\nu_\mu$ and $\bar{\nu}_\mu$ disappearance searches (46,40). The strongest constraint comes from combining MiniBooNE data with that from the SciBooNE detector, located a distance of 100 m from the neutrino source and having a 10.6-ton fiducial volume. SciBooNE was a scintillator tracking detector as opposed to the MiniBooNE mineral oil Cherenkov detector, but the neutrino and antineutrino cross sections, as well as the neutrino and antineutrino fluxes, are quite similar. The combined SciBooNE-MiniBooNE data have been used to set the world's best $\bar{\nu}_\mu$ disappearance limits for $\Delta m^2 < 20$ eV$^2$ (40).

### 5.2 Summary of Short Baseline Data Sets

In the next section, we will incorporate all data relevant to the high $\Delta m^2$ region into a single model. Figures 10, 11, and 12 show the data sets involved in the fits, presented as individual two-neutrino oscillation fits (Eqs. 3 and 4) (15). The data are categorized as $\nu_\mu \to \nu_e$ appearance searches, $\nu_\mu$ disappearance searches, and $\nu_e$ disappearance searches. Signals show up at 95% CL in the LSND, MiniBooNE, and Bugey reactor experiment (48) data sets. The reactor signal is a recent observation based on a reanalysis of the reactor flux (48). The other data sets have no closed contour at 95% CL, and so a limit is shown. However, it should be noted that the KARMEN/LSND cross section, discussed above in Sec. 5.1, and the Gallium data sets (49), from calibration data of SAGE (50) and GALLEX (51), both present closed contours at 90% CL.

Two issues for future analyses should be noted. First, if the Gallium data is corrected for recent estimates of the cross section (52), then the result would show a closed contour at 95% CL. Second, the MiniBooNE disappearance limits used in the global fits pre-date the final MiniBooNE-SciBooNE analyses (46, 40), and are slightly less stringent. However, we do not expect either of these issues to change significantly the overall conclusions of the next section.

## 6 LSND and MiniBooNE within the Context of Global Fits

We now present the LSND and MiniBooNE results within the context of global fits involving sterile neutrinos, following the phenomenology of Sec. 2. As described in Ref. (15), global fits are derived from Markov chain-based scans (47) from 0.01 $\mathrm{eV}^2$ to 100 $\mathrm{eV}^2$. Systematic and statistical errors are included.

We will quantify the quality of the fits through the $\chi^2$/dof and the compatibility of subsets through the Parameter Goodness-of-Fit (PGF) test (39). We will use two specific cases of the PGF test, dividing the data into appearance *vs.* disappearance data sets and neutrino *vs.* antineutrino data sets, using the respective definitions:

$$R_{PGF}^{appdis} = (\chi^2_{min,global} - \chi^2_{min,app} - \chi^2_{min,dis})/(N_{app} + N_{dis} - N_{global}) \qquad (9)$$

and

$$R_{PGF}^{\nu\bar{\nu}} = (\chi^2_{min,global} - \chi^2_{min,\nu} - \chi^2_{min,\bar{\nu}})/(N_{\nu} + N_{\bar{\nu}} - N_{global}). \qquad (10)$$

In the above, the numerator is a function of the minimum $\chi^2$ of the global fit and the subsets, while the denominator is a function of the number of independent parameters, $N$, in the corresponding fit. If the global best fit parameters are similar to those from the subset fits, then the $\chi^2_{PGF}$ value will be small and

will indicate good compatibility when the probability of $R_{PGF}$ is evaluated as a $\chi^2/dof$.

### 6.1 The Problem with 3+1 Fits

Referring to Sec. 2, a 3+1 fit has three parameters: $\Delta m^2_{41}$, $|U_{e4}|$ and $|U_{\mu 4}|$. The two matrix elements are related to the mixing angles according to Eqs. 5, 6, and 7.

Before fitting all of the data sets, a simple calculation can be used to show that the combined appearance and disappearance results from LSND and MiniBooNE alone already stress this model in the $\Delta m^2 > 1$ eV$^2$ region. In a 3+1 model, the mixing angle limit from the LSND-KARMEN cross section analysis translates to a limit on $|U^2_{e4}|$, through Eq. 7, that is roughly $\lesssim 0.05$, although there are large variations with $\Delta m^2$. The stringent $\sin^2 2\theta_{\mu\mu}$ limit from the MiniBooNE-SciBooNE joint analysis corresponds to $|U_{\mu 4}|^2 < 0.025$, using Eq. 6. Thus, the disappearance results favor a very small appearance mixing angle, which, from Eq. 5, is about $\sin^2 2\theta_{\mu e} \sim 0.005$ and is not in good agreement with LSND and MiniBooNE. Therefore, the LSND and MiniBooNE data alone will force a lower $\Delta m^2$ solution.

This is consistent with what is seen in the global fit (15), which yields a $\chi^2_{min}/dof$ of 233.9/237 with a 55% probability for this best fit point and a $\chi^2_{null}/dof$ of 286.5/240 with a 2.1% probability. The best fit parameters are 0.92 eV$^2$, 0.17, and 0.15, for $\Delta m^2$, $|U_{e4}|$, and $|U_{\mu 4}|$, respectively. Consequently, the $\Delta m^2$ of this solution sits just below 1 eV$^2$.

In contrast, the compatibility for this 3+1 model between appearance and disappearance (from Eq. 9) is found to be only 0.0013%, and the compatibility

between $\nu$ and $\overline{\nu}$ (from Eq. 10) is 0.14%. These very poor compatibilities are a warning that some data sets have best fit parameters in conflict with that found in the global fit. As a result, one is led to conclude that 3+1 models are, at best, marginal descriptions of the data.

## 6.2 Potential Success of 3+2 Global Fits

The poor compatibility of the data sets can possibly be improved by expanding to a 3+2 model, which introduces four new parameters: another high mass eigenstate, two additional mixing parameters, and a $CP$ phase. The latter allows for appearance signals for neutrinos that differ from antineutrinos. This extra degree of freedom significantly improves the compatibility between neutrino and antineutrino data sets, but it does not address the conflict between appearance and disappearance data sets.

From Ref. (15), the best fit parameters for a 3+2 model are: 0.92 eV$^2$, 17 eV$^2$, 0.13, 0.15, 0.16, 0.069, and $1.8\pi$, for the parameters $\Delta m^2_{41}$, $\Delta m^2_{51}$, $|U_{\mu 4}|$, $|U_{e4}|$, $|U_{\mu 5}|$, $|U_{e5}|$, and $\phi_{54}$ (the $CP$ phase), respectively. The results give good $\chi^2$ probabilities for a signal, with a $\chi^2_{min}/dof$ of 221.5/233 and a 69% probability for the best fit point and a $\chi^2_{null}/dof$ of 286.5/240 with a 2.1% probability–very similar to the 3+1 results. The PGF for the $\nu$ versus $\overline{\nu}$ data set comparison rises to 5.3%, which is acceptable.

It is striking, however, that the PGF for the appearance versus disappearance data sets slightly worsens from the 3+1 case to 0.0082%. The source of the issue can be tracked to the MiniBooNE low-energy excess. The fit to the $\nu$ and $\bar{\nu}$ appearance signals alone are internally consistent, assuming a non-zero $CP$ phase, but the best fit is strikingly different from the global fit. This can be

seen clearly in Fig. 13, where the MiniBooNE electron-like excess is shown for both neutrino and antineutrino modes and two example 3+2 fits are overlaid. The solid lines show the expectations for the global best fit. The dashed lines show the best fits to only the appearance data sets. The dashed lines indicate a good representation of the data, while the global fit cannot explain the rise in events at low energy. In fact, the parameter set for the appearance-only best fit is excluded by the disappearance data. Fig. 14 shows that, in contrast to MiniBooNE, the LSND appearance data set is in agreement with the 3+2 global fit. The normalization of LSND is approximately 30% higher than the global fit, but the energy-dependent shape is well described. Therefore, the poor PGF has been interpreted as indicating an issue with the MiniBooNE data in the global fits. For example, it has been suggested that multi-nucleon nuclear effects could cause the neutrino energy to be underestimated for some fraction of the events (59).

Rather than indicating a problem with the MiniBooNE data, however, this may instead be pointing to a limitation of the PGF description of compatibility. Consider Fig. 13 once again. After subtracting the 3+2 best fit prediction from the low-energy excess, the residual excess for neutrinos and antineutrinos can be fit to an enhanced $\pi^0$ background model. A 20% increase of the $\pi^0$ background normalization gives a $\chi^2/dof$ for the residual excess of 17.8/19. The systematic error on the MiniBooNE $\pi^0$ background is 14.5% (13.9% ) in neutrino (antineutrino) mode, and, therefore, this 20% discrepancy is only at the $1.4\sigma$ level. This is not a particularly large deviation, given the number of data sets in the global fit, and introduces concerns about the validity of the PGF compatibility statistic.

This apparent discrepancy may indicate that the PGF has difficulty properly

characterizing compatibility when systematic uncertainties can mimic a signal. The reason that the PGF is returning a poor compatibility can be seen from considering the numerator in Eq. 9. When appearance data are fit alone, a smaller $\chi^2$ is found when the entire MiniBooNE low-energy excess is attributed to an oscillation signal than when the global fit parameters plus a $1.4\sigma$ fluctuation of background are evaluated. This combination yields a large value for $R_{PGF}^{appdis}$, and hence a poor PGF, even though a compatible solution was available.

This 3+2 model can be tested in the near future, as it makes specific predictions for the MicroBooNE experiment (60), which will begin running in late 2013. The MicroBooNE experiment will use a liquid argon time projection chamber (LArTPC) 60 ton fiducial-volume, which will be located on the BNB close to the MiniBooNE detector. The LArTPC can differentiate events which have a final state electron from those with a final state photon. Unlike MiniBooNE, with LArTPC selection cuts, MicroBooNE will have very little contribution from photon-producing background sources, such as misidentified $\pi^0$ events. Thus, MicroBooNE will definitively show whether the MiniBooNE low-energy excess in neutrino mode is associated with electron neutrino events possibly from oscillations or events with photons from some other process.

## 7 Conclusions

Neutrino oscillations have been an unexpected and rich area for particle physics studies over the past several decades. The conclusive observations that neutrinos have mass and that lepton flavor is not conserved have changed the direction of the field. Now, the indications from LSND, MiniBooNE, and other experiments that a new type of sterile neutrino might exist could have an equally important impact.

Both LSND and MiniBooNE see indications of electron neutrino/antineutrino appearance, but there are discrepancies in the energy distributions of the appearance signal that could or could not be related to oscillations. The analysis of all high $\Delta m^2$ data sets shows that models with several sterile neutrinos can give acceptable global fits. Reported incompatibility with sterile neutrino models, especially between the appearance and disappearance measurements, may be arising from the choice of test statistic, rather than an underlying discrepancy with the data sets. Investigations of high $\Delta m^2$ oscillations currently form one of the most active areas of neutrino physics and many new experiments are being mounted or considered. This future program builds on the initial measurements of LSND and MiniBooNE discussed here and aims to provide a definitive exploration of new physics signals in the neutrino sector, such as sterile neutrinos.

## 8 Acknowledgments

This work was made possible by the dedicated efforts of the LSND and MiniBooNE collaborations. We thank C. Ignarra, G. Karagiorgi and Z. Pavlovic for their input. JMC and MHS thank the National Science Foundation for support. WL thanks the Department of Energy for support.

### Literature Cited

1. M. C. Gonzalez-Garcia, M. Maltoni, J. Salvado and T. Schwetz, arXiv:1209.3023 [hep-ph].
2. K. N. Abazajian *et al.*, arXiv:1204.5379 [hep-ph].
3. J. Beringer *et al.* [Particle Data Group], Phys. Rev. D **86**, 010001 (2012).
4. C. Athanassopoulos *et al.*, Phys. Rev. Lett. 75, 2650 (1995)

5. C. Athanassopoulos *et al.*, Phys. Rev. Lett. 77, 3082 (1996).

6. C. Athanassopoulos *et al.*, Phys. Rev. Lett. 81, 1774 (1998).

7. A. Aguilar *et al.*, Phys. Rev. D 64, 112007 (2001).

8. E. Church *et al.*, "A proposal for an experiment to measure $\nu_\mu \to \nu_e$ oscillations and $\nu_\mu$ disappearance at the Fermilab Booster: BooNE", submitted to the Fermilab Program Advisory Committee (1997).

9. A. A. Aguilar-Arevalo *et al.* [MiniBooNE Collaboration], [arXiv:0704.1500 [hep-ex]].

10. A. A. Aguilar-Arevalo *et al.* [MiniBooNE Collaboration], Phys. Rev. Lett. **103**, 111801 (2009) [arXiv:0904.1958 [hep-ex]].

11. A. A. Aguilar-Arevalo *et al.* [MiniBooNE Collaboration], arXiv:1207.4809 [hep-ex].

12. M. Sorel, J. M. Conrad and M. Shaevitz, Phys. Rev. D **70**, 073004 (2004).

13. G. Karagiorgi, A. Aguilar-Arevalo, J. M. Conrad, M. H. Shaevitz, K. Whisnant, M. Sorel and V. Barger, Phys. Rev. D **75**, 013011 (2007) [Erratum-ibid. D **80**, 099902 (2009)] [hep-ph/0609177].

14. G. Karagiorgi, Z. Djurcic, J. M. Conrad, M. H. Shaevitz and M. Sorel, Phys. Rev. D **80**, 073001 (2009) [Erratum-ibid. D **81**, 039902 (2010)].

15. J. M. Conrad, C. M. Ignarra, G. Karagiorgi, M. H. Shaevitz and J. Spitz, arXiv:1207.4765 [hep-ex].

16. F. P. An *et al.* [Daya Bay Collaboration], Phys. Rev. Lett. **108**, 171803 (2012); arXiv:1210.6327 [hep-ex].

17. Y. Abe *et al.* [Double Chooz Collaboration], Phys. Rev. D **86**, 052008 (2012) [arXiv:1207.6632 [hep-ex]].

18. S. Abe *et al.* [KamLAND Collaboration], Phys. Rev. Lett. **100**, 221803 (2008)

[arXiv:0801.4589 [hep-ex]].

19. P. Adamson *et al.* [MINOS Collaboration], Phys. Rev. Lett. **107**, 181802 (2011) [arXiv:1108.0015 [hep-ex]].

20. P. Adamson *et al.* [MINOS Collaboration], Phys. Rev. Lett. **108**, 191801 (2012) [arXiv:1202.2772 [hep-ex]].

21. J. K. Ahn *et al.* [RENO Collaboration], Phys. Rev. Lett. **108**, 191802 (2012) [arXiv:1204.0626 [hep-ex]].

22. R. Wendell *et al.* [Super-Kamiokande Collaboration], Phys. Rev. D **81**, 092004 (2010) [arXiv:1002.3471 [hep-ex]].

23. B. Aharmim *et al.* [SNO Collaboration], arXiv:1109.0763 [nucl-ex].

24. K. Abe *et al.* [T2K Collaboration], Phys. Rev. Lett. **107**, 041801 (2011) [arXiv:1106.2822 [hep-ex]].

25. K. Abe *et al.* [T2K Collaboration], Phys. Rev. D **85**, 031103 (2012) [arXiv:1201.1386 [hep-ex]].

26. R. L. Burman, M. E. Potter, and E. S. Smith, *Nucl. Instrum. Methods A* **291**, 621, (1990); R. L. Burman, A. C. Dodd, and P. Plischke, *Nucl. Instrum. Methods in Phys. Research A* **368**, 416, (1996).

27. C. Athanassopoulos *et al.* [LSND Collaboration], Nucl. Instrum. Meth. A **388**, 149 (1997) [nucl-ex/9605002].

28. J. J. Napolitano *et. al.* , *Nucl. Instrum. Methods A* **274**, 152, (1989).

29. A. A. Aguilar-Arevalo *et al.*, Phys. Rev. D 79, 072002 (2009).

30. A. A. Aguilar-Arevalo *et al.*, Nucl. Instrum. Meth. A 599, 28 (2009).

31. H. Gallagher, G. Garvey, and G.P. Zeller, Annu. Rev. Nucl. Part. Sci. **61**, 355 (2011)

32. This background also includes contributions from $\bar{\nu}_\mu C \to \mu^+ nX$ and $\nu_\mu C \to$

$\mu^- nX$.

33. G. Drexlin, *et al.*, Nucl. Instr. and Meth., A **289** 490 (1990).

34. B. Armbruster *et al.* [KARMEN Collaboration], Phys. Rev. D **65**, 112001 (2002) [hep-ex/0203021].

35. E. D. Church, K. Eitel, G. B. Mills, and M. Steidl, *Phys. Rev. D***66**, 013001, (2002).

36. A. A. Aguilar-Arevalo *et al.* [MiniBooNE Collab oration], [arXiv:0812.2243 [hep-ex]].

37. A. A. Aguilar-Arevalo *et al.* [MiniBooNE Collaboration], Phys. Rev. Lett. **105**, 181801 (2010) [arXiv:1007.1150 [hep-ex]].

38. G. Cheng *et al.* [SciBooNE Collaboration], Phys. Rev. D **84**, 012009 (2011) [arXiv:1105.2871 [hep-ex]], C. Mariani, G. Cheng, J. M. Conrad and M. H. Shaevitz, Phys. Rev. D **84**, 114021 (2011) [arXiv:1110.0417 [hep-ex]].

39. M. Maltoni and T. Schwetz, Phys. Rev. D **68**, 033020 (2003) [hep-ph/0304176].

40. G. Cheng *et al.*, arXiv:1208.0322 [hep-ex] (2012).

41. L. B. Auerbach *et al.* [LSND Collaboration], Phys. Rev. C **64**, 065501 (2001).

42. B. E. Bodmann *et al.* [KARMEN Collaboration.], Phys. Lett. B **332**, 251 (1994). B. Armbruster, *et al.* [KARMEN Collaboration], Phys. Rev. C57, 3414 (1998).

43. R. L. Burman, Nucl. Instrum. Meth. A **368**, 416 (1996).

44. R. L. Burman, M. E. Potter and E. S. Smith, Nucl. Instrum. Meth. A **291**, 621 (1990).

45. J. M. Conrad and M. H. Shaevitz, Phys. Rev. D **85**, 013017 (2012) [arXiv:1106.5552 [hep-ex]].

46. K. B. M. Mahn *et al.* [SciBooNE and MiniBooNE Collaboration], Phys. Rev. D **85**, 032007 (2012) [arXiv:1106.5685 [hep-ex]].

47. S. Hannestad, arXiv:0710.1952 [hep-ph].

48. G. Mention, M. Fechner, T. .Lasserre, T. .A. Mueller, D. Lhuillier, M. Cribier and A. Letourneau, Phys. Rev. D **83**, 073006 (2011) [arXiv:1101.2755 [hep-ex]].

49. M. A. Acero, C. Giunti and M. Laveder, Phys. Rev. D **78**, 073009 (2008) [arXiv:0711.4222 [hep-ph]].

50. J. N. Abdurashitov *et al.* [SAGE Collaboration], Phys. Rev. C **80**, 015807 (2009).

51. F. Kaether, W. Hampel, G. Heusser, J. Kiko and T. Kirsten, Phys. Lett. B **685**, 47 (2010).

52. C. Giunti and M. Laveder, Phys. Rev. C **83**, 065504 (2011) [arXiv:1006.3244 [hep-ph]].

53. P. Adamson *et al.*, Phys. Rev. Lett. **102**, 211801 (2009) [arXiv:hep-ex/0809.2447].

54. P. Astier *et al.* [NOMAD Collaboration], Phys. Lett. B **570**, 19 (2003) [arXiv:hep-ex/0306037]; D. Gibin, Nucl. Phys. Proc. Suppl. **66**, 366 (1998); V. Valuev [NOMAD Collaboration], http://www.slac.stanford.edu/spires/find/hep/www?irn=4920686SPIRES entry *Prepared for International Europhysics Conference on High-Energy Physics (HEP 2001), Budapest, Hungary, 12-18 Jul 2001.*

55. G. Cheng *et al.*, Phys. Rev. D **86**, 052009 (2012) [arXiv:hep-ex/1208.0322].

56. I. Stockdale *et al.* [CCFR Collaboration], Phys. Rev. Lett. 52, 1384 (1984), Z. Phys. C 27, 53 (1985).

57. F. Dydak *et al.*, Phys. Lett. B **134**, 281 (1984).

58. M. Maltoni, T. Schwetz, M. A. Tortola and J. W. F. Valle, New J. Phys. **6**, 122 (2004) [hep-ph/0405172].

59. M. Martini, M. Ericson, and G. Chanfray, arXiv:1202.4745 [hep-ph] (2012); O. Lalakulich and U. Mosel, arXiv:1208.3678 [nucl-th] (2012): J. Nieves, F. Sanchez, I. Ruiz Simo, and M. J. Vicente Vacas, arXiv:1204.5404 [hep-ph] (2012).

60. G. Karagiorgi [MicroBooNE Collaboration], J. Phys. Conf. Ser. **375**, 042067 (2012).

Table 1: Overview of the LSND and MiniBooNE experiments.

| Property | LSND | MiniBooNE |
|---|---|---|
| Proton Energy | 798 MeV | 8000 MeV |
| Proton Intensity | 1000 $\mu$A | 4 $\mu$A |
| Proton Beam Power | 798 kW | 32 kW |
| Protons on Target | 28,896 C | 284 C |
| Duty Factor | $6 \times 10^{-2}$ | $8 \times 10^{-6}$ |
| Total Mass | 167 tons | 806 tons |
| Neutrino Distance | 29.8 m | 541 m |
| Events for 100% $\nu_\mu \to \nu_e$ Transmutation | 33,300 | 128,077 |

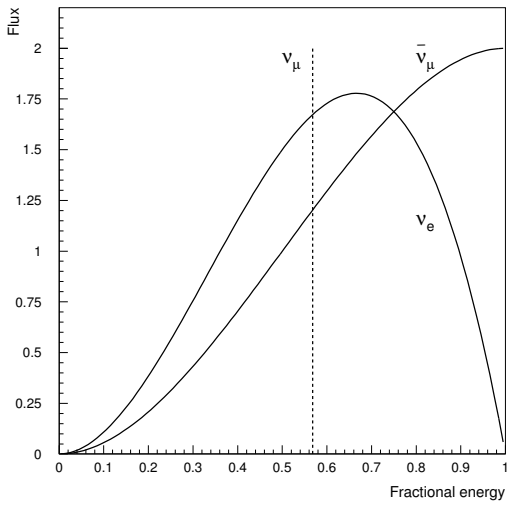


Figure 1: The neutrino energy spectra from $\pi^+$ and $\mu^+$ DAR.

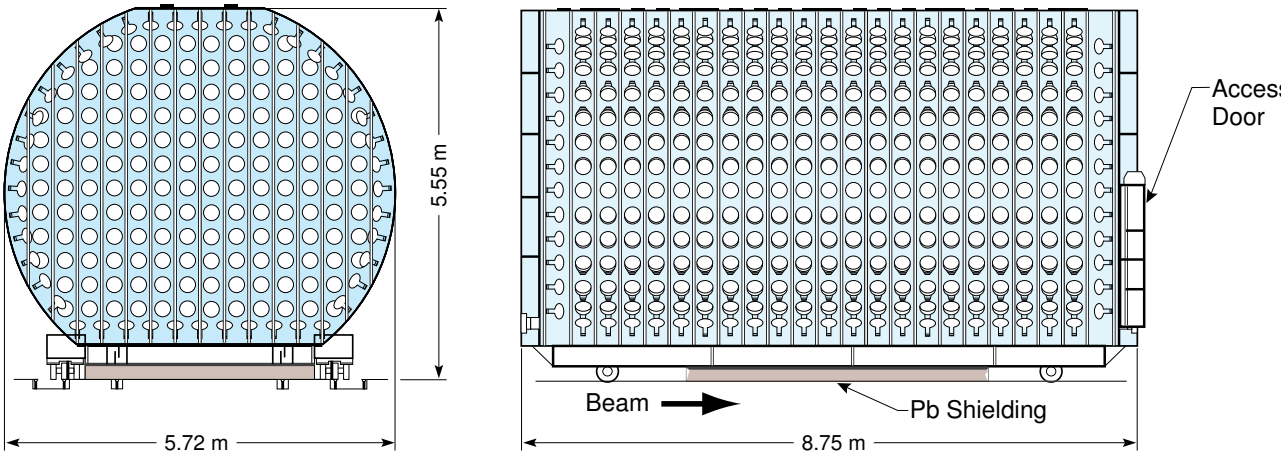


Figure 2: A schematic drawing of the LSND detector.

Table 2: Exercises in restricting the prompt events (7). The analysis used a right handed coordinate system with beam along $Z$ and $Y$ along the vertical axis. $D$ is distance from the PMT face.

| Selection | Oscillation Probability in % |
|---|---|
| Primary Analysis | $0.264 \pm 0.067 \pm 0.045$ |
| Primary + $D > 50$ cm and $Y > -50$ cm | $0.252 \pm 0.071 \pm 0.045$ |
| Primary + $D > 75$ cm | $0.193 \pm 0.055 \pm 0.045$ |
| Primary + $Y > -120$ cm | $0.293 \pm 0.069 \pm 0.045$ |

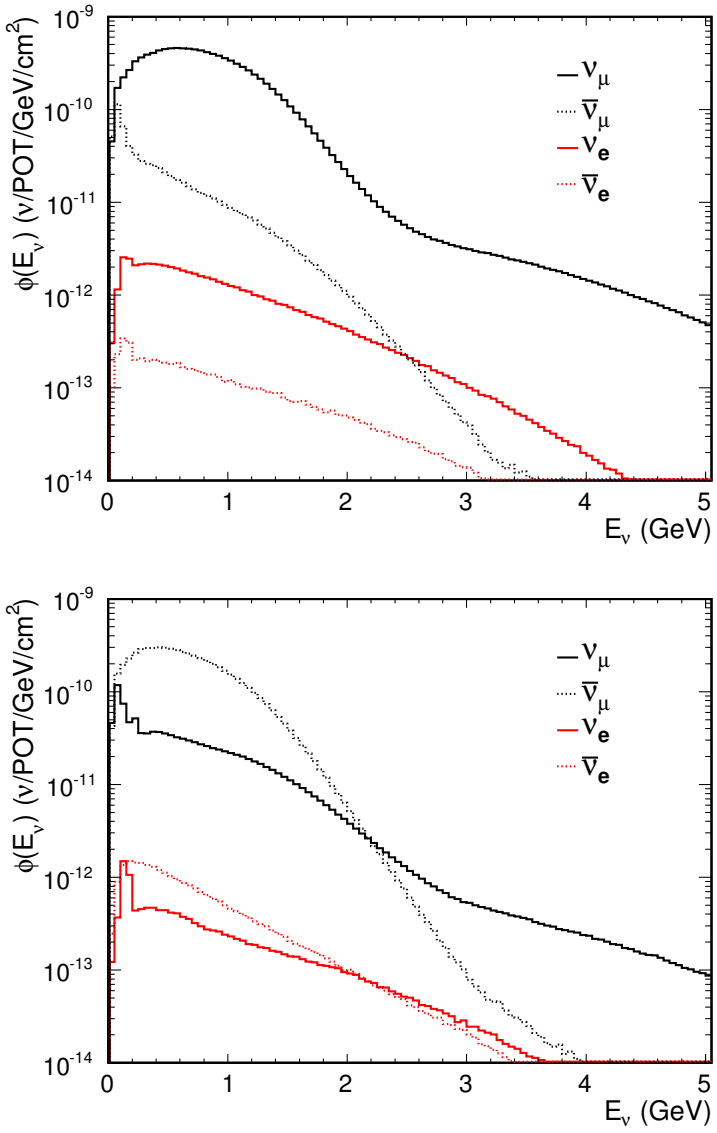


Figure 3: *The estimated neutrino fluxes for neutrino mode (top plot) and antineutrino mode (bottom plot).*

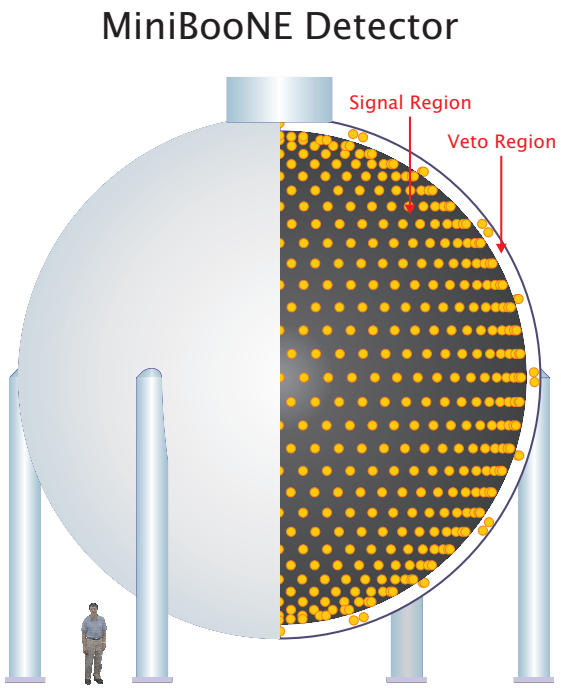


Figure 4: *A schematic drawing of the MiniBooNE detector.*

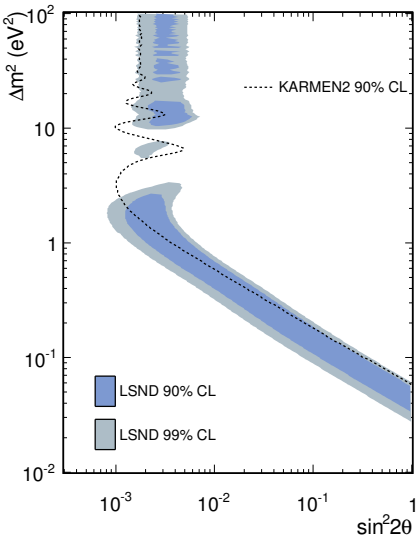


Figure 5: The $(\sin^2 2\theta, \Delta m^2)$ oscillation parameter fit for the entire LSND data set. The inner (outer) regions correspond to 90% (99%) CL allowed regions. 90% CL limits from the KARMEN2(34) experiments are also shown.

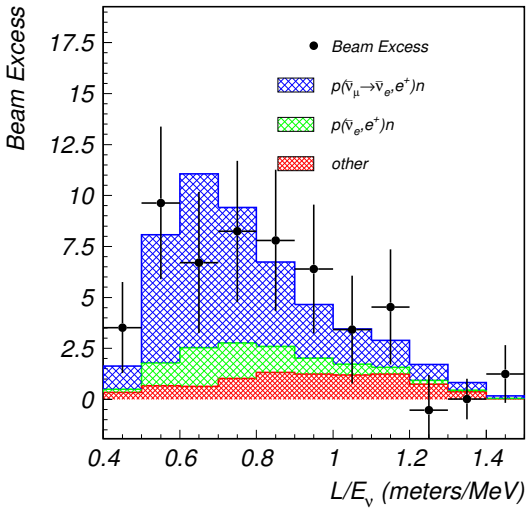


Figure 6: The LSND $L/E$ distribution for events with $R_\gamma > 10$ passing the Electron Selection criteria.

Table 3: *The MiniBooNE expected (unconstrained) number of events for the* $200 < E_\nu^{QE} < 1250$ *MeV neutrino oscillation energy range from all of the backgrounds in the* $\nu_e$ *and* $\bar{\nu}_e$ *appearance analysis and for the LSND expectation of 0.26% oscillation probability averaged over neutrino energy for both neutrino mode and antineutrino mode. Also shown are the total number of data events and the total constrained background (From Ref. (11).)*

| Process | Neutrino Mode | | Antineutrino Mode | |
|---|---|---|---|---|
| | 200-475 MeV | 475-1250 MeV | 200-475 MeV | 475-1 |
| $\nu_\mu$ & $\bar{\nu}_\mu$ CCQE | 25.4 | 11.7 | 8.8 | |
| NC $\pi^0$ | 181.2 | 71.1 | 85.4 | |
| NC $\Delta \to N\gamma$ | 66.9 | 19.9 | 26.4 | |
| External Events | 23.9 | 11.5 | 10.8 | |
| Other $\nu_\mu$ & $\bar{\nu}_\mu$ | 28.8 | 16.4 | 13.8 | |
| $\nu_e$ & $\bar{\nu}_e$ from $\mu^\pm$ Decay | 58.7 | 155.3 | 27.2 | |
| $\nu_e$ & $\bar{\nu}_e$ from $K^\pm$ Decay | 17.2 | 79.5 | 15.5 | |
| $\nu_e$ & $\bar{\nu}_e$ from $K_L^0$ Decay | 6.3 | 21.1 | 10.1 | |
| Other $\nu_e$ & $\bar{\nu}_e$ | 0.8 | 2.2 | 2.5 | |
| Total Unconstrained Background | 409.1 | 388.7 | 200.5 | 1 |
| 0.26% $\bar{\nu}_\mu \to \bar{\nu}_e$ | 50.4 | 182.7 | 23.7 | |
| Total Constrained Background | 401.3 | 388.8 | 203.3 | 1 |
| Number of Data Events | 544 | 408 | 257 | |

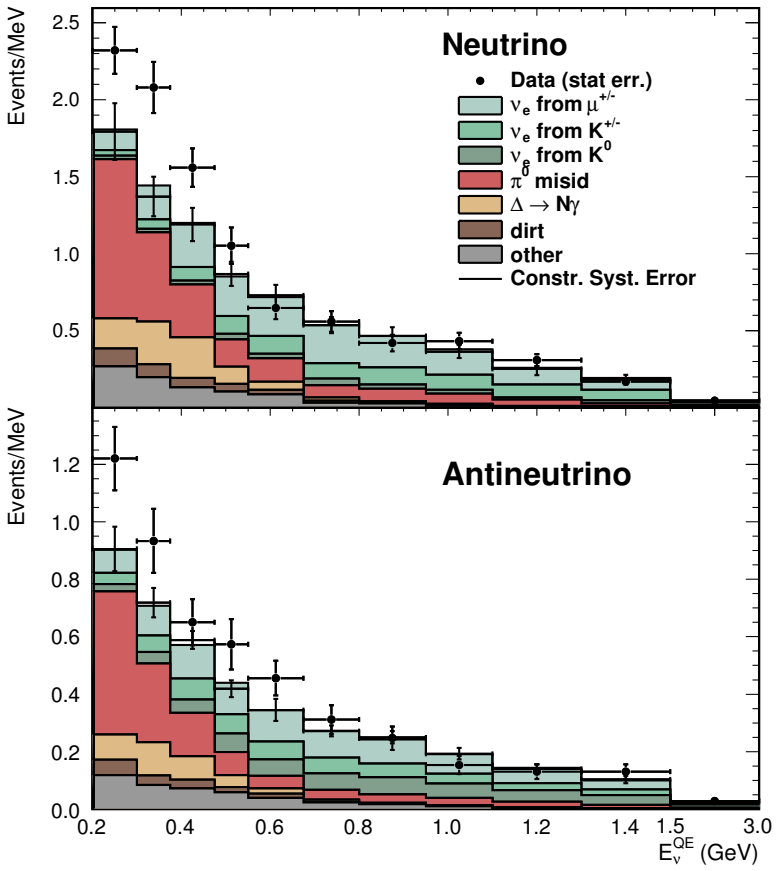


Figure 7: The neutrino mode (top) and antineutrino mode (bottom) $E_\nu^{QE}$ distributions for $\nu_e$ CCQE data (points with statistical errors) and background (histogram with systematic errors).

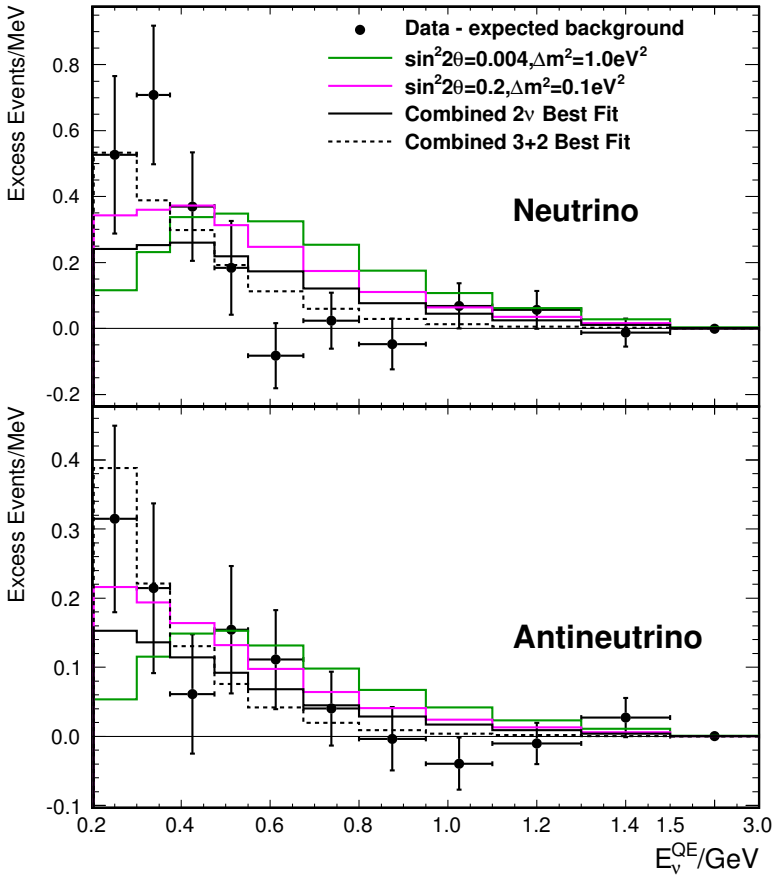


Figure 8: The neutrino mode (top) and antineutrino mode (bottom) event excesses as a function of $E_\nu^{QE}$. Also shown are the expectations from the best two-neutrino and 3+2 joint oscillation fits with $200 < E_\nu^{QE} < 3000$ MeV and from two reference values in the LSND allowed region. All known systematic errors are included in the systematic error estimate.

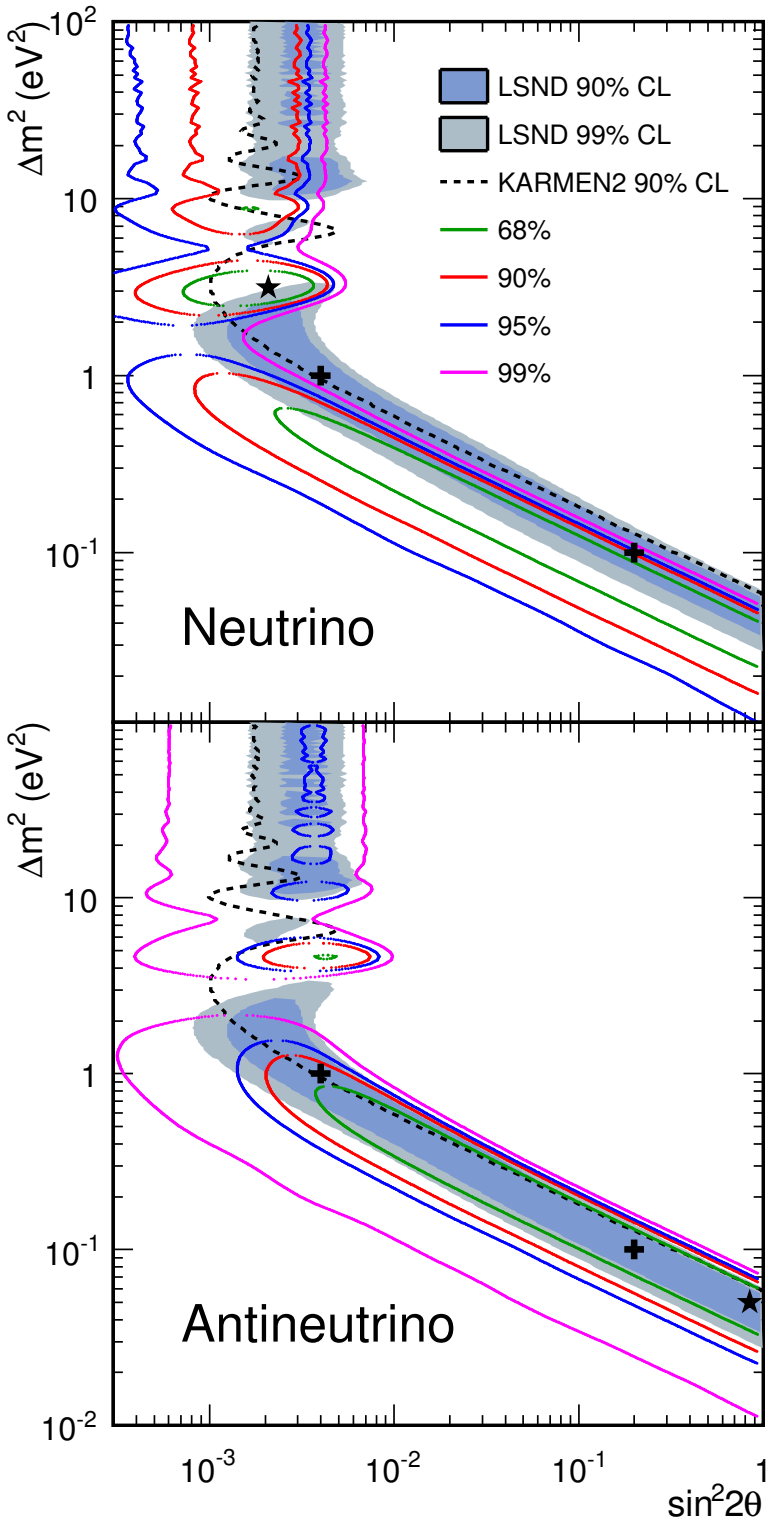


Figure 9: MiniBooNE allowed regions in combined neutrino and antineutrino mode for events with $200 < E_\nu^{QE} < 3000$ MeV within a two-neutrino $\nu_\mu \to \nu_e$ and $\bar{\nu}_\mu \to \bar{\nu}_e$ oscillation model. Also shown is the $\bar{\nu}_\mu \to \bar{\nu}_e$ limit from the KARMEN experiment (34). The shaded areas show the 90% and 99% CL LSND $\bar{\nu}_\mu \to \bar{\nu}_e$ allowed regions. The black star shows the best fit point.

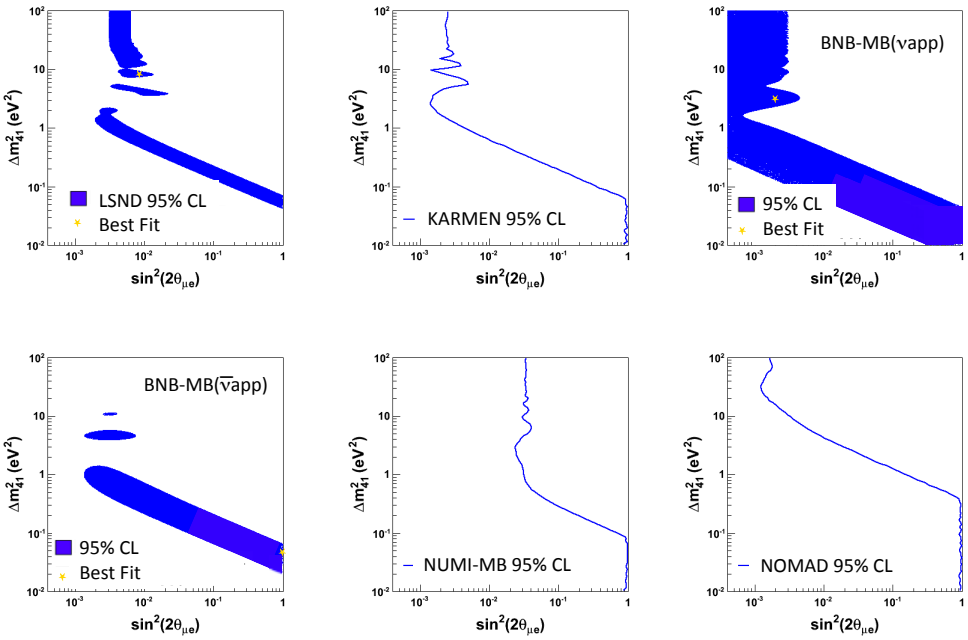


Figure 10: Summary of $\bar{\nu}_\mu \rightarrow \bar{\nu}_e$ and $\nu_\mu \rightarrow \nu_e$ results at 95% C.L. Top row: LSND (7), KARMEN (34), MiniBooNE with BNB beam, $\nu$ (9); Bottom row: MiniBooNE with BNB beam, $\bar{\nu}$ (11), MiniBooNE with NuMI beam (53), NOMAD (54). From Ref. (15).

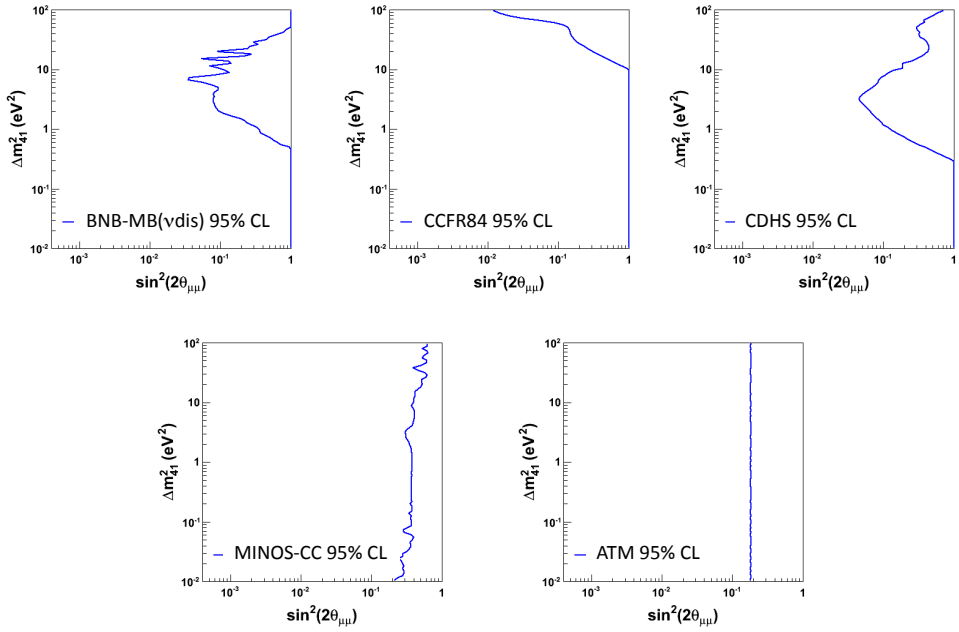


Figure 11: Summary of $\bar{\nu}_\mu \to \bar{\nu}_\mu$ and $\nu_\mu \to \nu_\mu$ results at 95% C.L. Top row: MiniBooNE $\nu$ (55), CCFR (56), CDHS (57); Bottom row: MINOS Charge Current data set (20), Atmospheric (58). From Ref. (15).

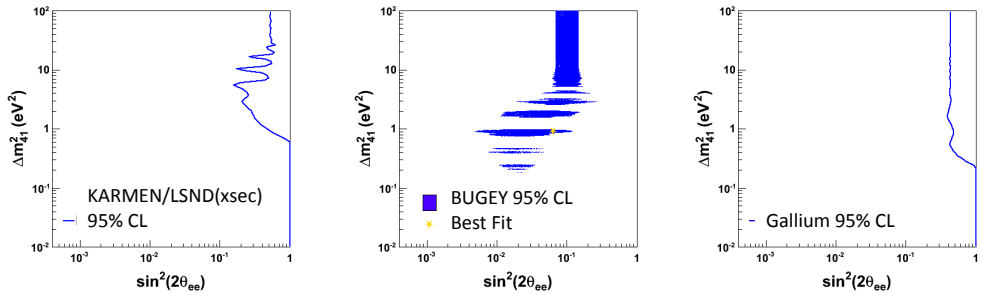


Figure 12: Summary of $\bar{\nu}_e \to \bar{\nu}_e$ and $\nu_e \to \nu_e$ results at 95% C.L. From left: KARMEN/LSND $\nu_e$ cross-section fit (45), Bugey (and other reactor experiments) (48), and Gallium (49). From Ref. (15).

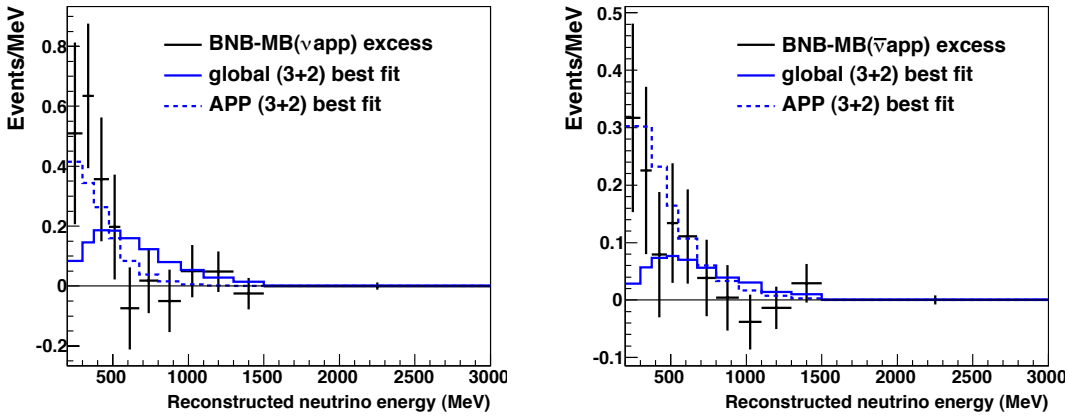


Figure 13: Illustration of the problem presented by the MiniBooNE data in global 3+2 fits to oscillations. Left, excess in neutrino mode; Right, excess in antineutrino mode. Solid line is global best fit; Dashed line is a 3+2 fit to only the appearance data (Plot from Ref. (15)).

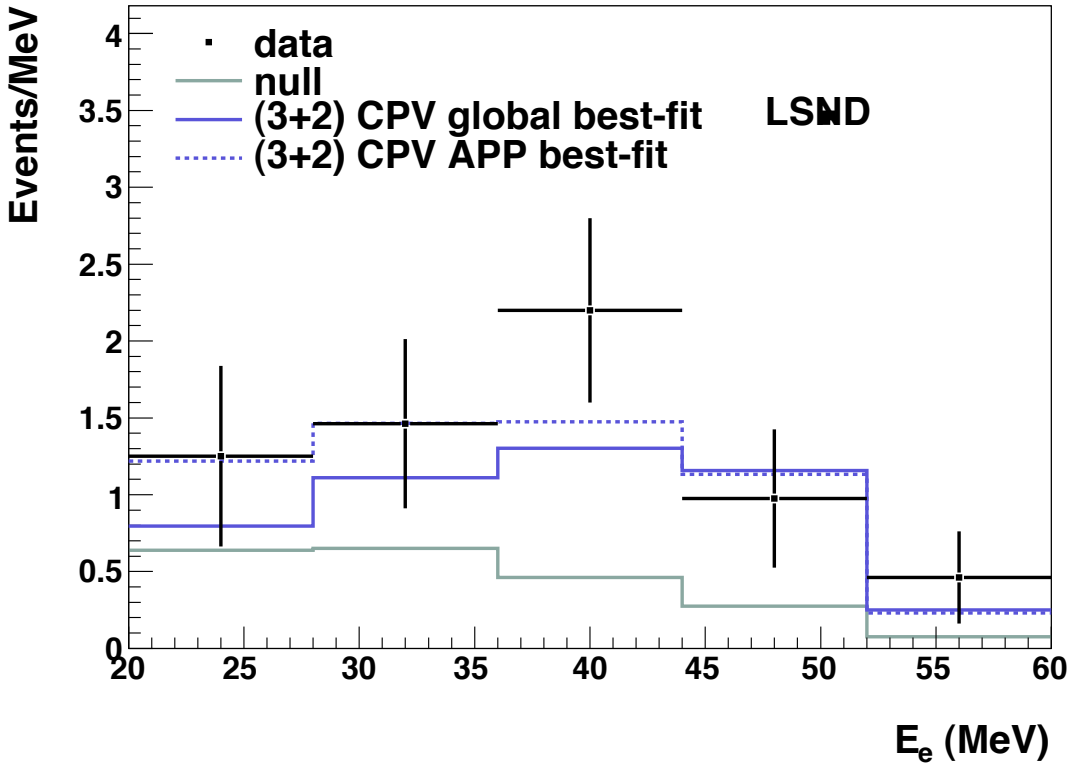


Figure 14: Comparison to the LSND data set of the global 3+2 fit to oscillations and the appearance-only fit.